Near room-temperature ferromagnetism from double exchange in the van der Waals material $CrGeTe_3$: Evidence from optical conductivity under pressure – Supplemental Material –

Jihaan Ebad-Allah,[1,2] Daniel Guterding,[3] Meera Varma,[1] Mangesh Diware,[4] Shraddha Ganorkar,[5] Harald O. Jeschke,[6] and Christine A. Kuntscher[1]

[1] *Experimentalphysik II, Institute for Physics, University of Augsburg, 86135 Augsburg, Germany*
[2] *Department of Physics, Tanta University, 31527 Tanta, Egypt*
[3] *Technische Hochschule Brandenburg, Magdeburger Straße 50, 14770 Brandenburg an der Havel, Germany*
[4] *Advanced Research Division, Park Systems Co., Suwon 16229, Republic of Korea*
[5] *School of Mechanical Engineering, Sungkyunkwan University, 2066 Seobu-ro, Jangan-gu, Suwon, Gyeonggi-do 16419, Republic of Korea*
[6] *Research Institute for Interdisciplinary Science, Okayama University, Okayama 700-8530, Japan*

I. SAMPLE PREPARATION, CHARACTERIZATION, AND CRYSTAL STRUCTURE

Single crystals of $CrGeTe_3$ were grown by using GeTe flux with a mixture of high purity powder of Cr, Ge, and Te at a molar ratio of 2:6:36, as described in detail in Refs. [1, 2]. The rhombohedral crystal structure of $CrGeTe_3$ with space group $R\bar{3}$ is depicted in Fig. S1. It consists of layers of a honeycomb network of edge sharing octahedra formed by a central Cr atom bonded to six Te atoms [1, 3].

Previous studies have explained ferromagnetism in $CrGeTe_3$ in terms of ferromagnetic superexchange mediated via the angle of the Cr-Te-Cr bonds that is close to 90 degrees [4, 5]. We show the pressure dependence of this angle in Fig. S2. The angle slightly increases with pressure, which could potentially lead to a weakening of ferromagnetic superexchange, as observed in the pressure range before the insulator-to-metal transition [2]. This weakening is not observed in our previous theoretical study [6], since DFT energy mapping takes into account all possible exchange paths, not just one. Ferromagnetic superexchange in a metal may, however, behave in a more complex way than a single leading-order term, as used in Ref. [2].

II. LOW-TEMPERATURE HIGH-PRESSURE INFRARED REFLECTIVITY MEASUREMENTS

High-pressure reflectance measurements during cooling down from 295 to 6 K were performed for pressures between 1.6 and 6.3 GPa and in the energy range from 0.0248 to 2.48 eV (200 to 20000 cm^{-1}). The measurements were carried out using an infrared microscope (Bruker Hyperion), equipped with a 15× Cassegrain objective, coupled to a Bruker Vertex 80v FT-IR spectrometer. A diamond anvil cell (DAC) from EasyLab company equipped with type IIA diamonds, which are suitable for infrared measurements, was utilized for pressure generation. For cooling, a Lake Shore continuous flow cryostat has been used. A freshly cleaved single crystal of $CrGeTe_3$, with the size of $\sim 160 \times 150 \times 40\ \mu m^3$, was loaded into the hole of a CuBe gasket inside the DAC. For ensuring the well-defined sample-diamond interface throughout the experiment, finely ground CsI powder was used as quasihydrostatic pressure transmitting medium. The pressure was determined *in situ* inside the cryostat using the ruby luminescence method [7, 8]. The pressure-dependent reflectivity spectra at the sample diamond interface R_{s-d} in the energy range 0.0248 to 1.116 eV (200 to 9000 cm^{-1}), were determined according to $R_{\text{s-d}}(\omega)=R_{\text{gasket-dia}}(\omega)\times(I_{\text{s}}(\omega)/I_{\text{gasket}}(\omega))$, where $I_s(\omega)$ is the intensity of the radiation reflected at the interface between the sample and the diamond anvil, $I_{\text{gasket}}(\omega)$ the intensity reflected from the CuBe gasket-diamond interface, and $R_{\text{gasket-dia}}(\omega)$ is the reflectivity of the gasket material for the diamond interface. While the R_{s-d} spectra in the energy range 1.116 to 2.248 eV (9000–20000 cm^{-1}) were calculated according to $R_{\text{s-d}}(\omega)=R_{\text{dia}}\times(I_{\text{s}}(\omega)/I_{\text{dia}}(\omega))$, where $R_{\text{dia}} = 0.167$ is the reflectivity of diamond, which was assumed to be pressure independent [9] and $I_{\text{dia}}(\omega)$ is the intensity reflected from the inner diamond-air interface of the empty DAC.

III. ANALYSIS OF REFLECTIVITY AND OPTICAL CONDUCTIVITY SPECTRA

To obtain the complex optical conductivity $\sigma(\omega)=\sigma_1(\omega)+i\sigma_2(\omega)$, the Kramers-Kronig relations were applied to transform the reflectivity spectra R_{s-d} to the various optical functions, taking the sample-diamond interface into account. The extrapolations of the R_{s-d} spectra were done in a manner similar to our previous publications [10–12]. To this end, Drude-Lorentz fitting procedures were applied for extrapolating the reflectivity data to zero frequency and interpolation in the frequency range 1800-2700 cm^{-1}, which is affected by multiphonon absorptions in the diamond anvils and not completely corrected by the normalization procedure. Above 2.5 eV, we used the high-energy extrapolation of the ambient-pressure reflectivity spectrum obtained by x-ray atomic scattering functions [13] after adjustment for the sample-

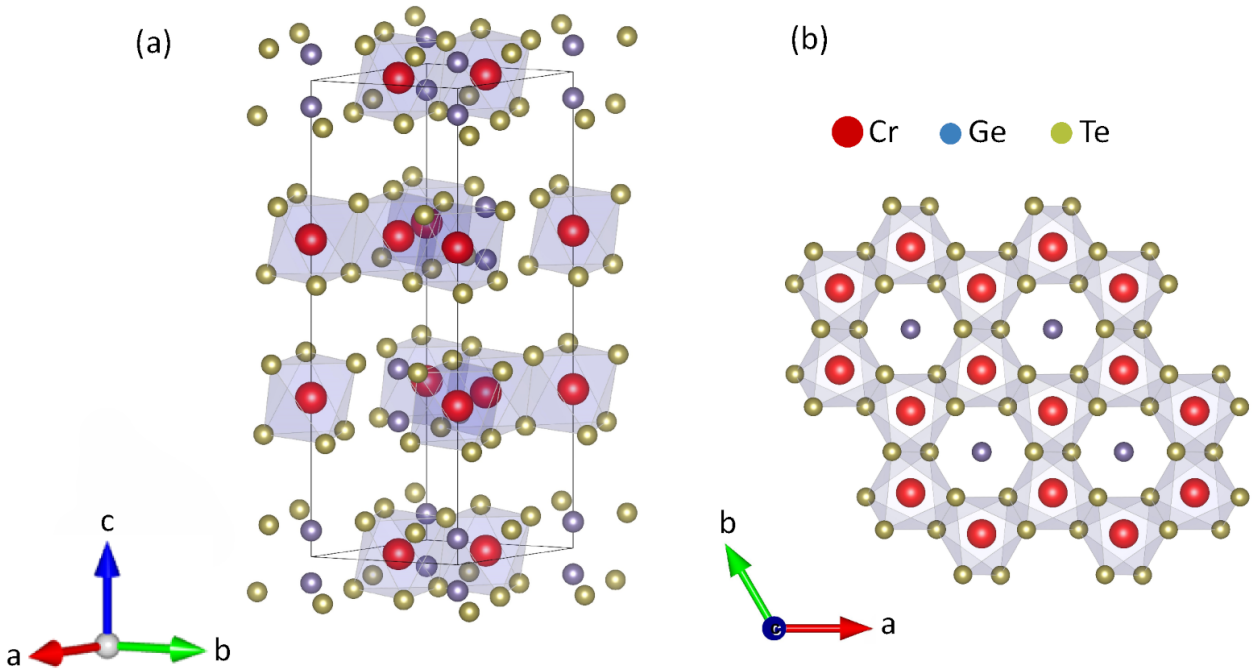

FIG. S1. Rhombohedral crystal structure of $CrGeTe_3$ with space group $R\bar{3}$ consisting of honeycomb layers with edge-sharing octahedra formed by a central Cr atom bonded to six Te atoms [1, 3].

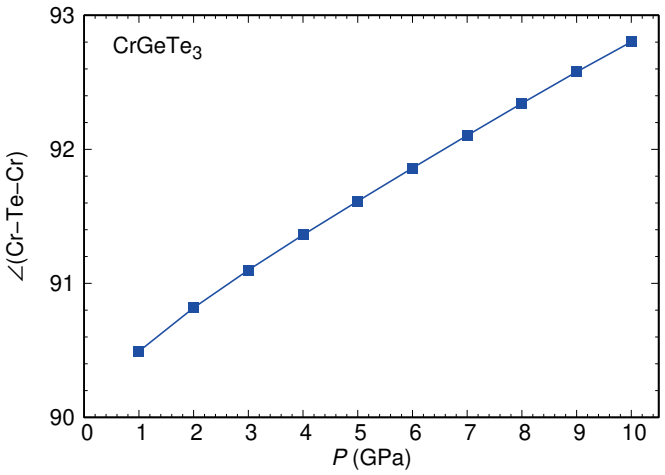

FIG. S2. Pressure evolution of the Cr-Te-Cr angle which corresponds to the nearest-neighbour exchange path J_1. Structures were interpolated as in Ref. [6].

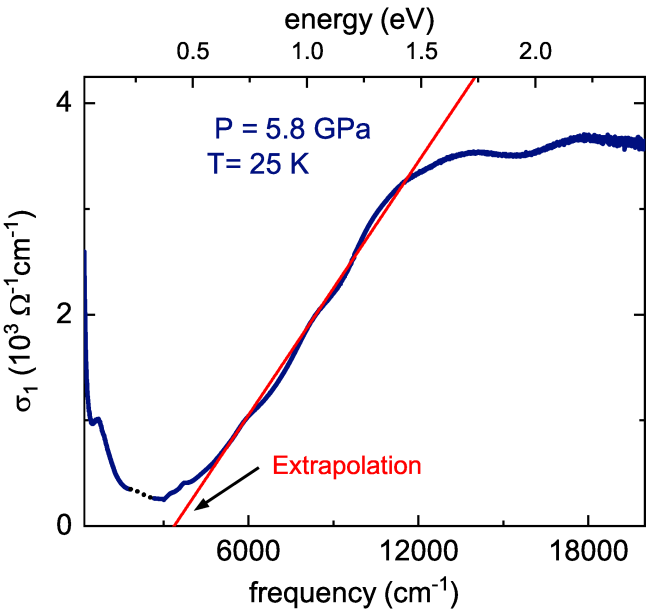

FIG. S3. Linear extrapolation of the absorption edge in the σ_1 spectrum at 25 K and 5.8 GPa as an example, for determining the charge-transfer gap size Δ_{CT}.

diamond interface. Furthermore, R_{s-d} and the optical conductivity were simultaneously fitted with the Drude-Lorentz model for decomposition of the σ_1 spectrum.

Within the Drude-Lorentz model the complex dielectric function $\epsilon(\omega) = \epsilon_1(\omega) + i\epsilon_2(\omega)$ is given as

$$\epsilon(\omega) = \epsilon_\infty - \frac{\omega^2_{\mathrm{p,Drude}}}{\omega^2 + i\omega/\tau_{\mathrm{Drude}}} + \sum_j \frac{\Omega_j^2}{\omega_{0,j}^2 - \omega^2 - i\omega\gamma_j} \quad , \tag{1}$$

where ϵ_∞ is the high-energy contribution to ϵ_1. $\omega_{\mathrm{p,Drude}}$ and $1/\tau_{\mathrm{Drude}}$ are the plasma frequency and scattering rate of itinerant charge carriers, respectively. $\omega_{0,j}$, Ω_j, and γ_j are the eigenfrequency, oscillator strength, and width of the j^{th} Lorentz oscillator, respectively. The decomposition of the σ_1 spectra into Drude and Lorentz

contributions as a function of pressure and temperature is given in Section X.

The charge-transfer gap size Δ_{CT} was estimated by a linear extrapolation of the absorption edge in the σ_1 spectrum, which is an accepted way in the literature [14–17]. We illustrate the procedure in Fig. S3 for the conductivity spectrum at 25 K and 5.8 GPa.

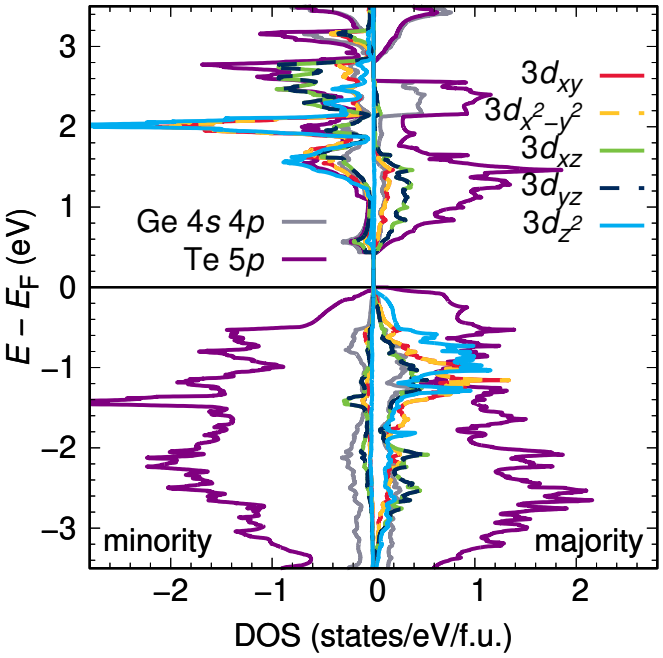

FIG. S4. Orbital-resolved density of states of $CrGeTe_3$ at ambient pressure (P = 0 GPa) in the ferromagnetic state calculated using DFT.

IV. DENSITY FUNCTIONAL THEORY CALCULATIONS

For the interpretation of the observed excitations in the optical conductivity spectra, we perform density functional theory (DFT) calculations within the full potential local orbital (FPLO) method [18] in generalized gradient approximation (GGA) [19] for the exchange-correlation functional. We used experimental crystal structures for $CrGeTe_3$ under pressure from Ref. [20], which we interpolated smoothly as explained in Ref. [6]. All calculations were performed in ferromagnetic spin configuration.

We calculated the partial density of states (DOS) in the ferromagnetic state at ambient pressure (P = 0 GPa) from FPLO using a $50 \times 50 \times 50$ k-point grid. The results are shown in Fig. S4. The density of states is dominated by Cr 3d and Te 5p orbitals, with additional contributions from Ge 4s and 4p states. Te and Ge states are present for both the majority and minority spins. The Cr 3d orbitals are spin split and mostly occupied for the majority spin, while being mostly unoccupied for the minority spin.

The optical conductivity in the main text was calculated using the FPLO density functional theory code on a $50 \times 50 \times 50$ k-point grid. For the figures in the supplemental material, we modified the FPLO code to obtain the interband contribution to the symmetric (in band indices) band-resolved optical conductivity tensor $[\sigma^{\pm}_{xx}(\omega)]_{ij}$, where i and j are band indices, which run over all bands in the FPLO basis, and $+/-$ stands for the majority/minority spin. The band-resolved optical conductivity tensor was calculated on a coarser $20 \times 20 \times 20$ k-point grid (for performance reasons). We verified that a sum over the band indices of this tensor reproduces the result of the unmodified code. Alternatively, we could have calculated the orbital-resolved optical conductivity tensor, which would have required extensive changes to the FPLO DFT code and caused further numerical effort. Therefore, we chose not to pursue this route.

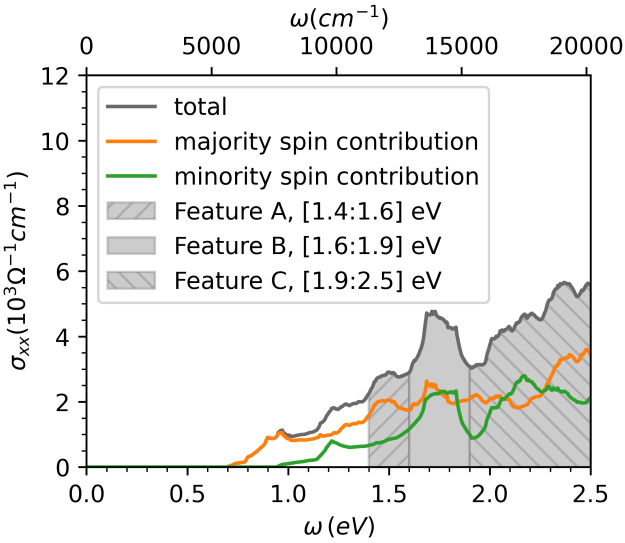

FIG. S5. Spin contributions to the σ_{xx} component of the optical conductivity of $CrGeTe_3$ at P = 0 GPa in the ferromagnetic state calculated using DFT. We relate the shaded energy windows to the observed features A, B and C of the measured optical conductivity.

We calculated the spin-resolved optical conductivity $\sigma^{\pm}_{xx}(\omega)$ at ambient pressure (P = 0 GPa) using the FPLO method, with *ab-initio* interband transition matrix elements. The total optical conductivity is defined as the sum of the majority and minority spin component: $\sigma_{xx}(\omega) = \sigma^{+}_{xx}(\omega) + \sigma^{-}_{xx}(\omega)$. The results are shown in Fig. S5. We shaded the energy regions in which we observe three distinct features that are similar to the experimentally observed optical conductivity. These are feature A in the energy region $[1.4 : 1.6]$ eV, feature B in the energy region $[1.6 : 1.9]$ eV and feature C in the energy region $[1.9 : 2.5]$ eV. Under pressure, these features are shifted very slightly, but the qualitative picture remains unchanged. The calculated optical conductivity is in good agreement with experimental data.

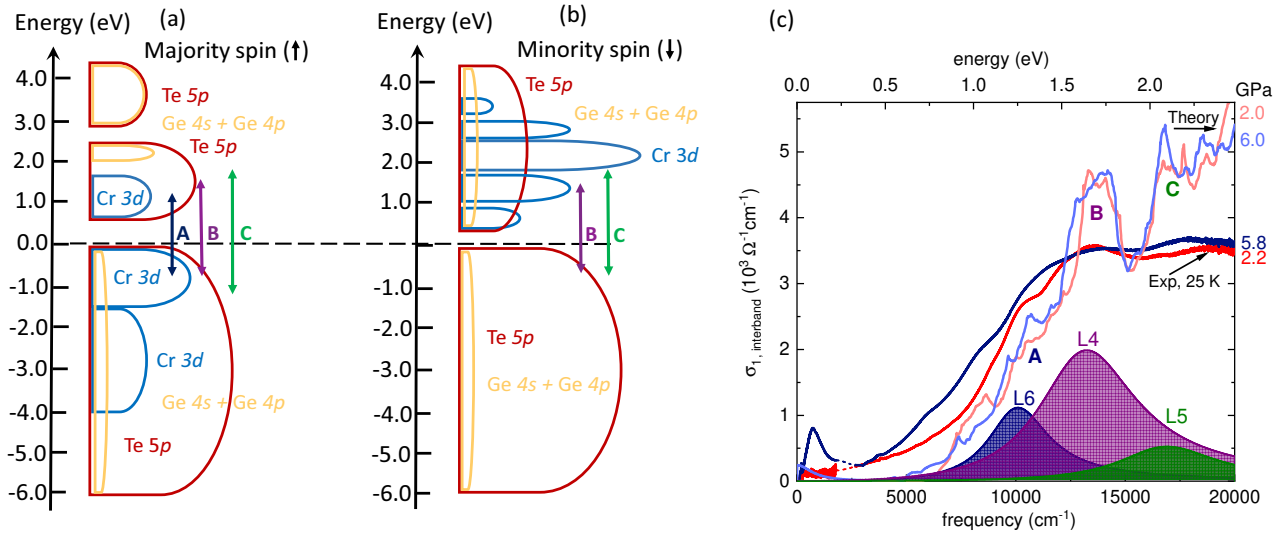

FIG. S6. Energy scheme of $CrGeTe_3$ for (a) majority and (b) minority spin. The vertical arrows mark the possible electronic transitions, which explain the three interband excitations A, B and C. (c) Comparison between the experimental and theoretical interband conductivity $\sigma_{1,\,\mathrm{interband}}$ at 2.2 and 5.8 GPa and at 25 K, i.e., within the ferromagnetic phase, together with the fit contributions L4, L5, and L6 at 2.2 GPa.

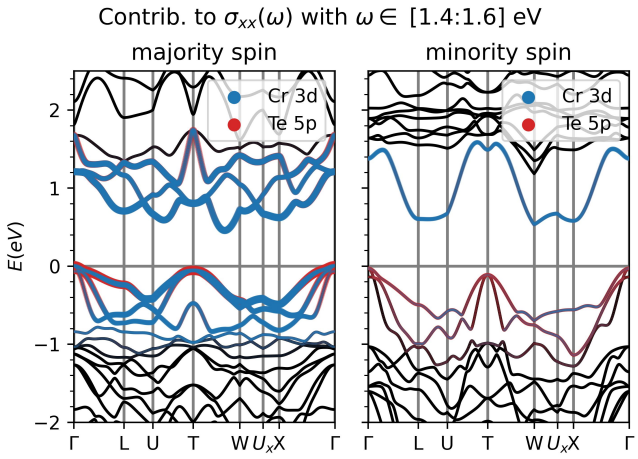

FIG. S7. DFT-calculated spin-resolved electronic band structure of $CrGeTe_3$ at P = 0 GPa in the ferromagnetic state with orbital weights multiplied by the relative contributions of each band to the optical conductivity in the energy window [1.4:1.6] eV (feature A).

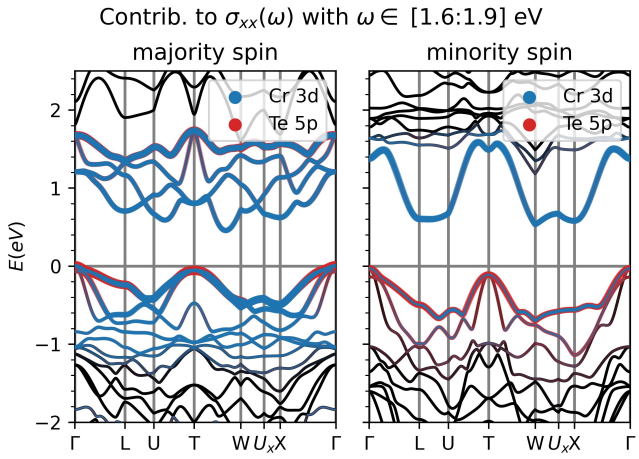

FIG. S8. DFT-calculated spin-resolved electronic band structure of $CrGeTe_3$ at P = 0 GPa in the ferromagnetic state with orbital weights multiplied by the relative contributions of each band to the optical conductivity in the energy window [1.6:1.9] eV (feature B).

The experimental optical conductivity at 25 K contains three prominent features (see Fig. 2(d) in main text) at around 1.3 eV (A), 1.6 eV (B) and 2.1 eV (C). Under pressure, an additional absorption band arises below 200 meV. The main three features A, B, and C can be explained based on our DFT calculations (see Fig. S5). Feature A is dominated by transitions between Cr 3*d* and Te 5*p* states with majority spin. Features B and C are explained by transitions between Cr 3*d* and Te 5*p* states with both majority and minority spin. The dip in the calculated optical conductivity between features B and C follows from a gap between minority spin Cr 3*d* states above the Fermi level. These transitions are indicated in the schematic DOS in Fig. S6. A previous DFT study of ambient pressure $CrGeTe_3$ predicted similar features in the optical conductivity, but at energies above 2 eV [21].

In the following, we visualize the contributions of each band to the optical conductivity in the specific energy regions. In addition to the standard band weights $b_{ij}^{\pm}(\vec{k})$, which represent the weight of orbital j to band i at

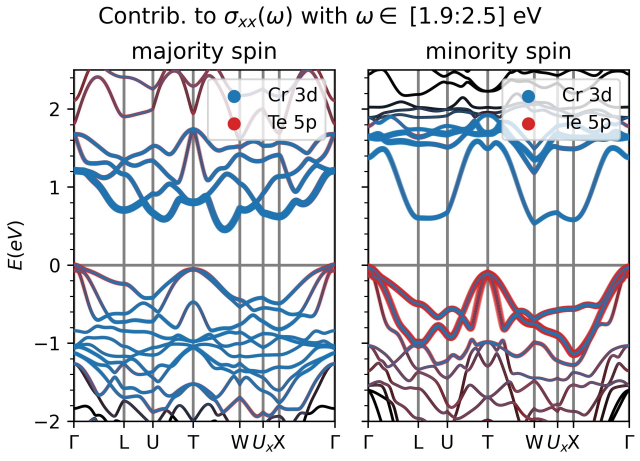

FIG. S9. DFT-calculated spin-resolved electronic band structure of $CrGeTe_3$ at P = 0 GPa in the ferromagnetic state with orbital weights multiplied by the relative contributions of each band to the optical conductivity in the energy window [1.9:2.5] eV (feature C).

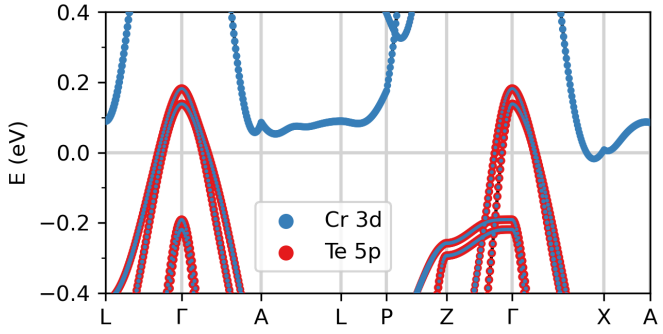

FIG. S10. Full-relativistic electronic band structure of $CrGeTe_3$ in the ferromagnetic state calculated from DFT at a pressure of 5 GPa. The chosen k-path differs from other band structure plots, so that both hole and electron pockets are easily recognizable.

a k-point $\vec{k}$, we calculate multiplicative band weights $c_i^{\pm}(\omega_{\min}, \omega_{\max}) \in [0, 1]$ for each band i and energy interval $\omega \in [\omega_{\min}, \omega_{\max}]$ of the optical conductivity. For this, we integrate over the frequency parameter of the optical conductivity tensor:

$$[\sigma_{xx}^{\pm}]_{ij}(\omega_{\min}, \omega_{\max}) = \int_{\omega_{\min}}^{\omega_{\max}} d\omega \, [\sigma_{xx}^{\pm}(\omega)]_{ij} \quad . \tag{2}$$

The raw weight of each band is then given by the sum over one of the band indices of the tensor:

$$\begin{aligned} \tilde{c}_i^{\pm}(\omega_{\min}, \omega_{\max}) &= \sum_j [\sigma_{xx}^{\pm}]_{ij}(\omega_{\min}, \omega_{\max}) \\ &= \sum_j \int_{\omega_{\min}}^{\omega_{\max}} d\omega \, [\sigma_{xx}^{\pm}(\omega)]_{ij} \quad . \end{aligned} \tag{3}$$

For convenience of visualization, we normalize these raw weights so that they faithfully represent the relative contribution of each band to the optical conductivity in the energy region of interest:

$$c_i^{\pm}(\omega_{\min}, \omega_{\max}) = \frac{\tilde{c}_i^{\pm}(\omega_{\min}, \omega_{\max})}{\max\left(\tilde{c}_i^{+}(\omega_{\min}, \omega_{\max}), \tilde{c}_i^{-}(\omega_{\min}, \omega_{\max})\right)} \, . \tag{4}$$

The band weights $a_{ij}^{\pm}(\vec{k}, \omega_{\min}, \omega_{\max})$ we visualize in the following are given by the product of the standard orbital weight $b_{ij}^{\pm}(\vec{k})$ and our custom weight $c_i^{\pm}(\omega_{\min}, \omega_{\max})$:

$$a_{ij}^{\pm}(\vec{k}, \omega_{\min}, \omega_{\max}) = b_{ij}^{\pm}(\vec{k}) \cdot c_i^{\pm}(\omega_{\min}, \omega_{\max}) \quad . \tag{5}$$

Here, i is the band index, while j is the orbital index. Since the weights $c_i^{\pm}(\omega_{\min}, \omega_{\max})$ are zero for any bands which do not contribute to the optical conductivity in the energy window $[\omega_{\min}, \omega_{\max}]$, this multiplication filters out bands which are irrelevant for the optical conductivity in the respective energy window. Important bands will be represented by weights proportional to their contribution to the optical conductivity as defined above. Our results for the three energy windows identified in Fig. S5 are shown in Figs. S7, S8 and S9.

Our analysis clearly differentiates the contributions of majority and minority spin electrons and also allows us to analyze the region of active bands for the optical conductivity, as well as the contribution of each orbital to these bands. In Figs. S7-S9, we only show orbital weights for Cr 3d and Te 5p orbitals. Ge 4s and 4p and any other weights on the relevant bands are relatively small, as can be seen by comparing the band structure to the orbital-resolved density of states (see Fig. S4 and also Fig. S6).

As explained in the main text, the calculated optical conductivity does not change dramatically with pressure, even though the material becomes metallic. At ambient pressure, $CrGeTe_3$ has an indirect band gap. Under pressure, the system becomes metallic, but the band gap closes only indirectly (see Fig. S10). Since optical transitions do not transfer momentum, *i.e.* they occur vertically in our electronic band structure diagrams, the interband contribution to the optical conductivity remains zero at low excitation energies due to the vertical gap between highest occupied and lowest unoccupied band at each k-point.

V. DENSITY FUNCTIONAL THEORY + DYNAMICAL MEAN-FIELD THEORY CALCULATIONS

We performed DFT + dynamical mean-field theory (DFT+DMFT) calculations within `DCORE` [22] for the electronic structure of $CrGeTe_3$, as explained in Ref. [6]. The one-body Hamiltonian extracted from DFT via projective Wannier functions [23] in FPLO [18] is a 36-band model. These bands include states from two formula units of $CrGeTe_3$, comprising 10 Cr 3d, 18 Te 5p, 2 Ge

4s and 6 Ge 4p orbitals. The resulting energy window ranges from −9.5 eV to +4.5 eV.

We use the hybridization expansion continuous-time quantum Monte Carlo (CT-QMC) method to solve the DMFT impurity problem [24, 25]. The Hartree-Fock approximation is used to estimate the double-counting correction based on the bare Green's function. We use a slight reduction of the double-counting correction by 4%, as for CeB_6 [26]. We consider correlations only between electrons on the Cr 3d orbitals so that the local self-energy has non-zero matrix elements only on the diagonals that represent the 3d orbitals on each Cr atom.

In the single-impurity Anderson model, we only consider density-density terms in the Kanamori-type interaction, which is given by

$$\begin{aligned}\mathcal{H}_{\text{int}} = & U \sum_{\alpha} n_{\alpha\uparrow} n_{\alpha\downarrow} + U' \sum_{\sigma} n_{1\sigma} n_{2\bar{\sigma}} \\ & + (U' - J_{\text{H}}) \sum_{\sigma} n_{1\sigma} n_{2\sigma} \quad ,\end{aligned} \tag{6}$$

where $\bar{\sigma}$ stands for the spin component opposite to σ. The inter-orbital Coulomb interaction U' is determined from U and J by $U' = U - 2J_{\text{H}}$. The intra-orbital Coulomb interaction U and the Hund's rule coupling J_{H} are fixed at $U = 2\,\text{eV}$ and $J_{\text{H}} = 0.72\,\text{eV}$.

We performed the DMFT self-consistency calculations using `DCORE` [22] implemented on the TRIQS library [27]. The single-impurity problem was solved using an implementation [28] of the hybridization-expansion CT-QMC method [24, 25] integrated into `DCORE`. Summations over $\boldsymbol{k}$ and ω_n are performed with $n_k = 20^3$ points and $n_{iw} =$ 9000 points (for positive frequencies) at $T = 100\,\text{K}$.

Our previous analysis of the DFT+DMFT spectral function in the ferromagnetic state at T = 100 K and P = 5 GPa (see Fig. 5d and 5e in Ref. [6]) shows a feature at around +200 meV for the minority spin electrons that is almost flat in momentum space. A corresponding feature appears in the majority spin spectral function around -200 meV (see Fig. 5e and 5f in Ref. [6]).

We performed additional analysis of the electronic self-energy of $CrGeTe_3$ to explain these features of the spectral function. We can clearly identify the peaks at ±200 meV in the DFT+DMFT spectral function with peaks in the DFT+DMFT electronic self-energy for the Cr 3d_{z^2} orbital (Fig. S11). The imaginary part of the self-energy resembles a doped Mott-insulator [29–32], although the energy difference between the two features suggests that these are not Hubbard bands. The spin-spliting is induced by the ferromagnetism and resembles previous theoretical results [33].

Therefore, the peaks in the spectral function at ±200 meV can be interpreted as correlation-induced features of the Cr 3d_{z^2} orbital. We conjecture that the formation of these features in the spectral function is related to minority spins subject to unfavorable Hund's rule interaction, which in turn stabilizes the double-exchange mechanism (see below). Certainly, we can identify the mid-infrared (MIR) feature of the optical conductivity

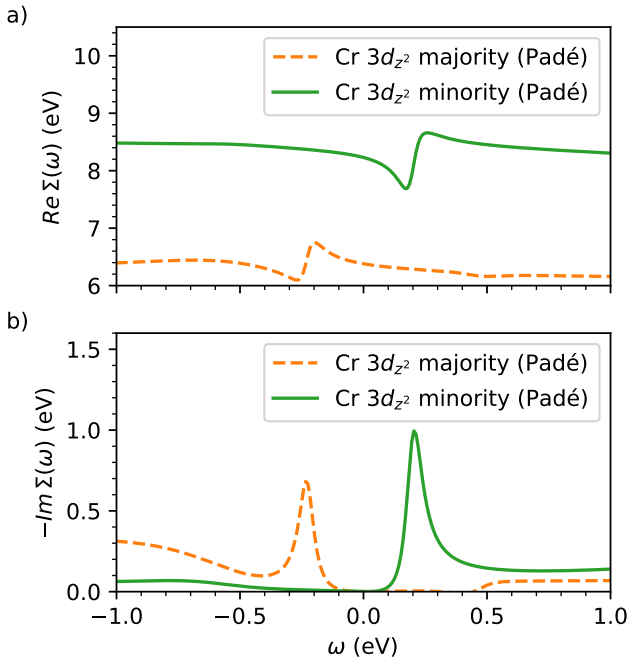

FIG. S11. DFT+DMFT self-energy on the real frequency axis $\Sigma(\omega)$ for the majority- and minority-spin Cr 3d_{z^2} orbital of $CrGeTe_3$ at T = 100 K and P = 5 GPa in the ferromagnetic state. Results are shown for the Padé analytic continuation method. a) shows the real part of the self-energy $\text{Re}\,\Sigma(\omega)$. b) shows the imaginary part of the self-energy $-\text{Im}\,\Sigma(\omega)$.

as a transition of minority-spin electrons from below the Fermi level to this correlation-induced peak of the Cr 3d_{z^2} spectral function above the Fermi level.

The discussion above applies to a pressure of P = 5 GPa. At lower pressures, $CrGeTe_3$ is an insulator. Pressure induces a transition from an insulator to a correlated ferromagnetic metal due to the creation of holes in the majority-spin states and electrons in the minority-spin states of chromium, as well as an overall increase in Cr 3d occupancy (see Fig. 12 in Ref. [6]). Therefore, we believe that the inherent occupation imbalance of majority and minority spin Cr 3d states under pressure helps to avoid an insulating state.

We verified that the feature in the self-energy at an energy of about +200 meV is not an artifact of the analytic continuation procedure, which is employed when working with CT-QMC impurity solvers. In Ref. [6] we used the Padé method for analytic continuation [34], which is known to capture well at least the features close to the Fermi level. Here, we additionally used the recently developed sparse modeling (SpM) analytic continuation method [35], which may improve the accuracy at higher energies.

As expected, the electronic self-energy of the minority spin Cr 3d_{z^2} orbital is similar in both methods (see Fig. S12). While the Padé result shows only one major feature in both the real and imaginary part of the

TABLE S1. DFT+DMFT quasiparticle weights for $CrGeTe_3$ and other compounds. In case two values are given for the quasiparticle weight, these represent the values for the majority/minority spin states. For references containing temperature-dependent values for the quasiparticle weight, we take the value corresponding to the lowest available temperature. For orbitals not listed in our table, the cited references did not contain any values for the quasiparticle weight.

compound	$CrGeTe_3$ ($P = 5$ GPa) [6]	VSe_2 [36]	CoS_2 [37]	$NiSe_2$ [38]
weakly correlated orbitals	Cr $3d_{xy}$, $d_{x^2-y^2}$, d_{xz}, d_{yz}	V $3d_{xz}$, d_{yz}	Co $3d_{xy}$, d_{xz}, d_{yz}	Ni $3d_{xy}$, d_{xz}, d_{yz}
quasiparticle weight	~ 0.8	~ 0.65	1.0	1.0
strongly correlated orbitals	Cr $3d_{z^2}$	V $3d_{z^2}$, d_{xy}, $d_{x^2-y^2}$	Co $3d_{z^2}$, $d_{x^2-y^2}$	Ni $3d_{z^2}$, $d_{x^2-y^2}$
quasiparticle weight	~ 0.6 / ~ 0.45	~ 0.4	0.83 / 0.59	~ 0.5
compound	$SrNiO_2$ [39]	$LaNiO_2$ [39]	$NdNiO_2$ [40]	CrI_3 monolayer [41]
weakly correlated orbitals	Ni $3d_{z^2}$, d_{xy}, d_{xz}, d_{yz}	Ni $3d_{z^2}$, d_{xy}, d_{xz}, d_{yz}	Ni $3d_{z^2}$	Cr $3d_{xy}$, d_{xz}, d_{yz}
quasiparticle weight	~ 0.66	~ 0.81	~ 0.77	~ 0.5 / ~ 0.42
strongly correlated orbitals	Ni $3d_{x^2-y^2}$	Ni $3d_{x^2-y^2}$	Ni $3d_{x^2-y^2}$	Cr $3d_{z^2}$, $d_{x^2-y^2}$
quasiparticle weight	0.53	0.36	~ 0.34	~ 0.58 / ~ 0.25

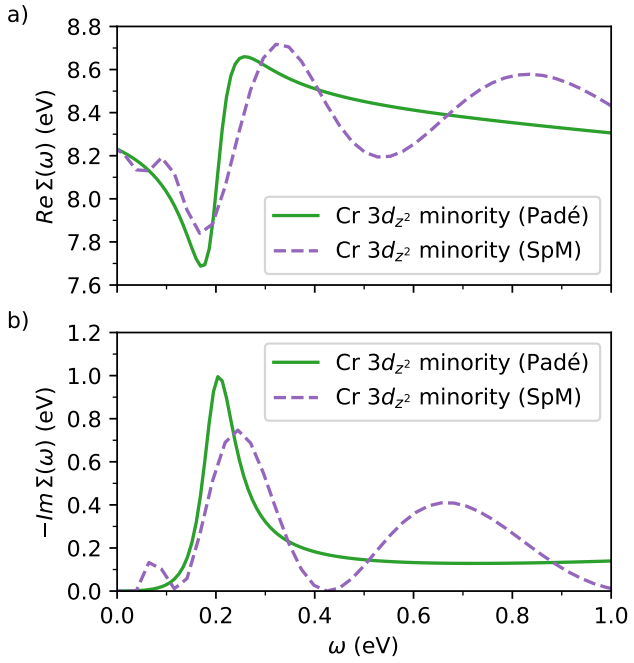

FIG. S12. DFT+DMFT self-energy on the real frequency axis $\Sigma(\omega)$ for the minority-spin Cr $3d_{z^2}$ orbital of $CrGeTe_3$ at T = 100 K and P = 5 GPa in the ferromagnetic state. Results are shown for both Padé and sparse modeling (SpM) analytic continuation methods. a) shows the real part of the self-energy $\mathrm{Re}\,\Sigma(\omega)$. b) shows the imaginary part of the self-energy $-\mathrm{Im}\,\Sigma(\omega)$.

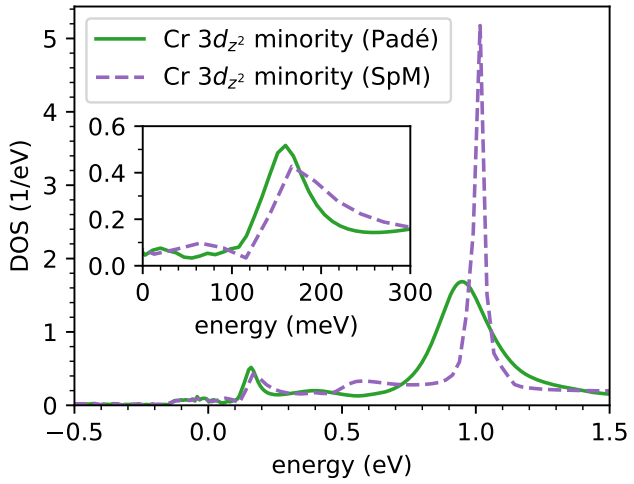

FIG. S13. DFT+DMFT spectral function for the minority-spin Cr $3d_{z^2}$ orbital of $CrGeTe_3$ at T = 100 K and P = 5 GPa in the ferromagnetic state. Results are shown for both Padé and sparse modeling (SpM) analytic continuation methods. The inset shows the low-energy feature, which persists independently of the continuation method.

self-energy, the SpM result contains additional minor features.

Therefore, the spectral function of the minority spin Cr $3d_{z^2}$ orbital is very similar in both methods (see Fig. S13). As expected, the low-energy region of the spectral function is almost identical. The hump in the k-integrated spectral function around +200 meV, which we believe is observed in the experimental optical conductivity under pressure, is present irrespective of the analytic continuation method. Minor differences only appear at energies higher than about +0.5 eV, which the Padé method often does not capture in all detail. This does not affect any of the conclusions of our previous calculations for $CrGeTe_3$ (see Ref. [6]).

To estimate the correlation strength in $CrGeTe_3$ at 5 GPa in our DFT+DMFT calculations, we calculate the quasiparticle-weight z_σ^m, where σ denotes the spin and m denotes the orbital index, from the electronic self-energy Σ_σ^m at the lowest positive Matsubara frequency ω_0 [42]. The quasiparticle weight is also the inverse of the mass enhancement over a pure DFT calculation due to correlations, *i.e.* the effective mass m^* divided by the DFT

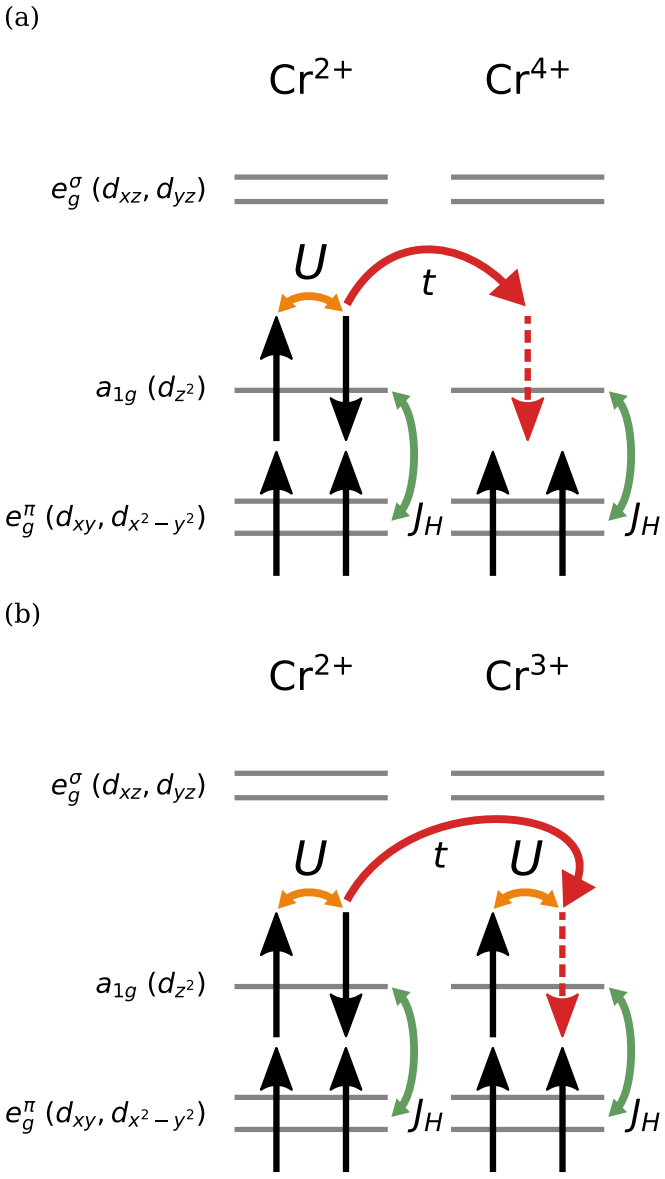

FIG. S14. Schematic depiction of exchange processes relevant for minority spin Cr $3d_{z^2}$ electrons. (a) Hopping of a minority spin electron into a majority spin d_{z^2} hole. (b) Hopping of a minority spin electron onto an occupied majority spin d_{z^2} site.

band mass m_{DFT}:

$$(z_\sigma^m)^{-1} = 1 - \frac{\mathrm{Im}\,\Sigma_\sigma^m(\omega_0)}{\omega_0} = \frac{m^*}{m_{\mathrm{DFT}}} \quad . \tag{7}$$

Effects of electronic correlations among the Cr $3d$ orbitals in $CrGeTe_3$ are strongly orbital-selective [6]. The minority spin a_{1g} (d_{z^2}) electrons are strongly correlated under pressure, as demonstrated by a decreased quasiparticle weight of about 0.45, which leads to a substantial mass enhancement. The majority spin a_{1g} orbital is slightly less correlated, with a quasiparticle weight of about 0.6. The e_g^π (d_{xy}, $d_{x^2-y^2}$) and e_g^σ (d_{xz}, d_{yz}) orbitals are weakly correlated with a quasiparticle weight of about 0.8. This hierarchy of correlations reflects the trigonal crystal field of $CrGeTe_3$, where a_{1g} (d_{z^2}) electrons are closest to the Fermi level for a nominal Cr^{3+} configuration. The strength of electronic correlations in $CrGeTe_3$ under pressure, as measured by the quasiparticle weight, is similar to theoretical results for transition metal dichalcogenides [36–38] and nickelates [39, 40, 43], while monolayers of transition metal trihalides appear to be more strongly correlated [41] (see Table S1).

We note here that our microscopic picture of majority spin holes and minority spin electrons combined with local interactions also explains the strong differentiation of effective masses by orbitals and spins in $CrGeTe_3$. Since the Cr $3d_{z^2}$ orbital is closest to half filling and fully polarized, its electrons are most impeded by electron-electron correlations. The creation of holes in the majority spin Cr $3d_{z^2}$ orbital not only mobilizes the majority spin electrons, but also increasingly localizes the minority spin Cr $3d_{z^2}$ electrons in the vicinity of these holes, since they can lower their energy by hopping into a hole, where they are only subject to Hund's rule coupling (see Fig. S14(a)), but avoid the Coulomb repulsion of a doubly occupied site (see Fig. S14(b)). Since the energy cost of spin misalignment with respect to Hund's rule coupling J_H (see Fig. S14(a)) is roughly equal to the distance of both peaks in the spectral function (at ±200 meV), it seems possible that Hund's rule coupling is responsible for these low-energy features of the electronic self-energy (see Fig. S11(b)).

VI. ANALYSIS OF THE LINEAR MODEL FOR CURIE TEMPERATURE VERSUS PLASMA FREQUENCY

Mean-field analysis [44] of the Anderson and Hasegawa double-exchange Hamiltonian [45] yields a linear relationship between the Curie temperature and the squared plasma frequency ω_p^2. As shown in the main text, a linear function $T_\mathrm{C}(\omega_\mathrm{p}^2) = a \cdot \omega_\mathrm{p}^2 + b$ is clearly consistent with our data. Due to the small number of data points and large temperature error bars, naturally we can not exclude that other relations between T_C and ω_p^2 may fit the data equally well or even better.

As an alternative to the linear relationship, we tested a power law $T_\mathrm{C}(\omega_\mathrm{p}^2) = a \cdot (\omega_\mathrm{p}^2)^k + b$. We added the constant term b to account for other contributions, such as from superexchange. For each value of exponent k, we numerically optimized the coefficients a and b to minimize the mean squared deviation between the model and our experimental data. We used all our experimental data points with non-zero plasma frequency. The fit error was calculated both with equal weights and weighted by the inverse of the error of the Curie temperature. These two approaches yield only minor differences. Subsequently, we calculated the standard coefficient of determination R^2, which is close to one if a model is consistent with the data.

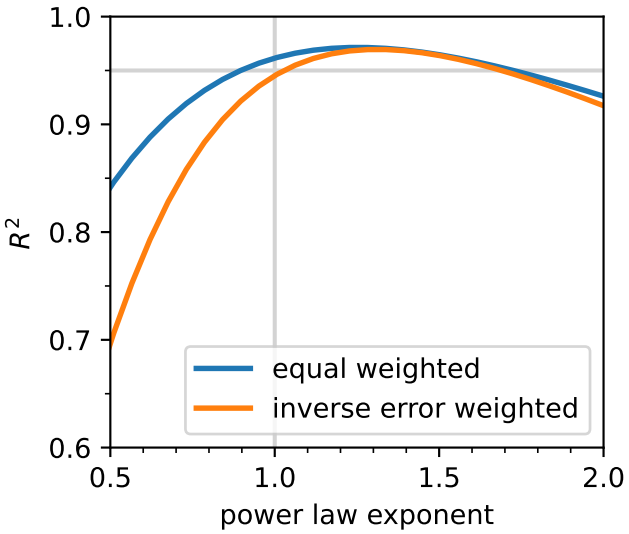

FIG. S15. Coefficient of determination R^2 as a function of the exponent k in the power law $T_C(\omega_p^2) = a \cdot (\omega_p^2)^k + b$. An R^2 value close to one means that the model is consistent with the data. Coefficients a and b were determined to optimally fit the experimental T_C based on the experimental squared plasma frequency ω_p^2.

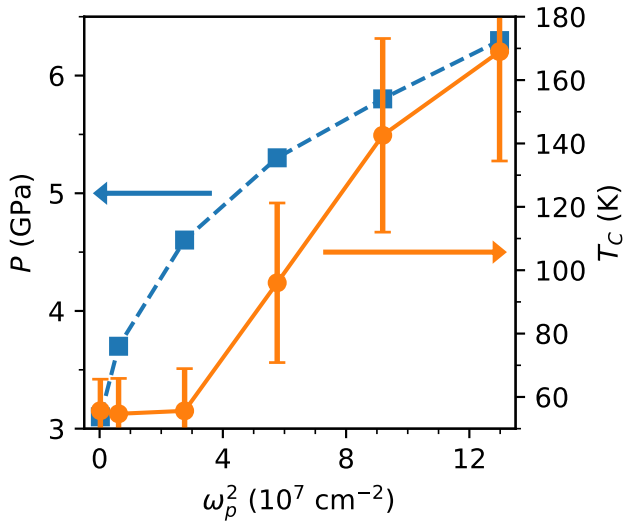

FIG. S16. Pressure P (left axis) and Curie temperature T_C (right axis, from Ref. [2]) versus squared plasma frequency ω_p^2. While our data are consistent with a linear relation between Curie temperature and plasma frequency, the pressure and squared plasma frequency are not related in a linear way. This creates a nonlinearity when mapping the modeled Curie temperature back to the physical pressure axis.

Our results in Fig. S15 show that there is a whole range of such power law models which is consistent with our data. If we require that $R^2 \geq 0.95$, we find that good models, for which the quality of fit is nearly indistinguishable, have an exponent k in the range from 0.9 to about 1.7. The weighting with the inverse of the errors of T_C gives a slightly smaller range, shifted a little to larger exponents. To narrow the range of acceptable exponents down, we would need to conduct additional experiments at various pressures in the metallic phase, also requiring smaller error bars for the Curie temperature. Nevertheless, we can say that the linear model ($k = 1$) is in very good agreement with our data.

In Fig. 4(c) in the main text, the double-exchange model, which is a linear function of the plasma frequency, picks up a slight nonlinearity when plotted as a function of physical pressure. This is because the squared plasma-frequency and pressure are not connected by a linear relation. This is most easily seen by plotting both pressure and Curie temperature as a function of the squared plasma frequency. From the results in Fig. S16 it is clear that a nonlinearity can be expected in a plot of Curie temperature versus pressure.

VII. DECREASING CHARGE-TRANSFER GAP AS AN ALTERNATIVE EXPLANATION FOR THE ENHANCED CURIE TEMPERATURE

As an alternative to the double-exchange model that we have put forward, an enhancement of the Curie temperature due to enhanced superexchange interaction J_{SE} upon decrease of the charge-transfer gap Δ has been suggested in the literature [2].

Based on our measurements of the charge-transfer gap, we can give an estimate of the enhancement factor. The superexchange interaction can be written in terms of the p-d hoppings t, the Hund's rule coupling J_H^{Te} on the Te site, the Coulomb repulsion U_p on the Te site and the charge-transfer gap Δ [2]:

$$J_{\mathrm{SE}} \propto \frac{t_{pd}^2 t_{p'd'}^2 J_H^{\mathrm{Te}}}{\Delta^2 (2\Delta + U_p)^2} \quad . \tag{8}$$

As the Curie temperature in the insulating regime stays almost constant around 50 K under pressure, where the charge-transfer gap is almost constant, we conclude that the hoppings, Hund's rule coupling and Coulomb repulsion must be almost constant under pressure, unless there is some unlikely cancellation of trends at play.

If we now assume that all parameters except the charge-transfer gap Δ are constant as a function of pressure, we may estimate the enhancement η of the superexchange interaction, when the gap decreases from Δ to a smaller value Δ':

$$\eta = \frac{J'_{\mathrm{SE}}}{J_{\mathrm{SE}}} = \left(\frac{\Delta}{\Delta'} \frac{2\Delta + U_p}{2\Delta' + U_p} \right)^2 \quad . \tag{9}$$

For example, we calculated the enhancement factor from a pressure of about 3 GPa, where the charge-transfer gap is close to $\Delta = 0.65$ eV to a pressure of about 6 GPa,

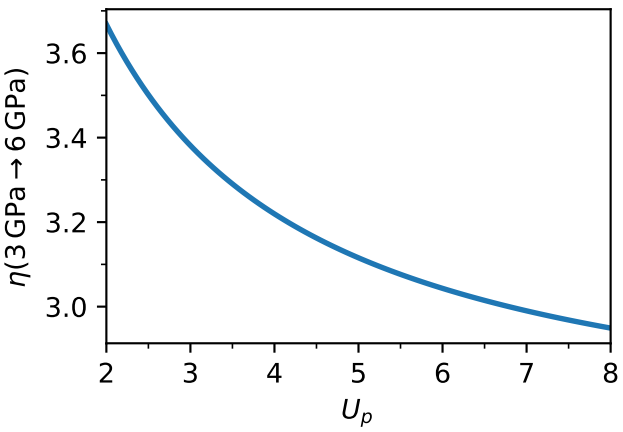

FIG. S17. Hypothetical enhancement η of the superexchange interaction J_{SE} due to the decreasing charge-transfer gap as a function of the Coulomb repulsion U_p on the Te site.

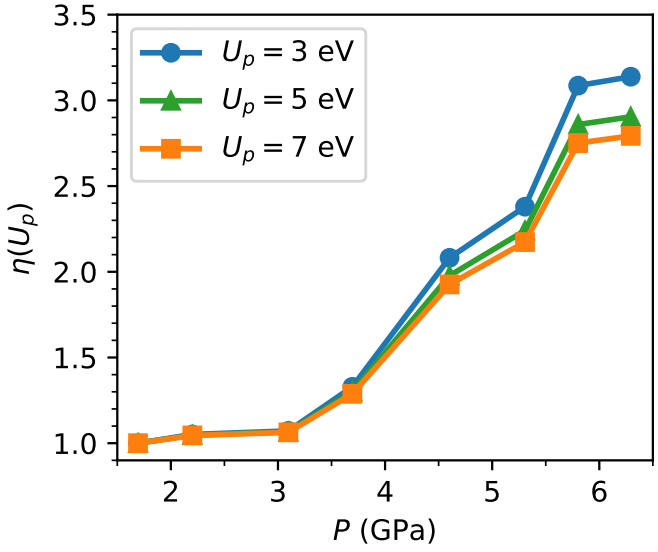

FIG. S18. Hypothetical enhancement η of the superexchange interation J_{SE} due to the decreasing charge-transfer gap as a function of pressure for various values of the Coulomb repulsion U_p on the Te site.

where the charge-transfer gap is close to $\Delta' = 0.4$ eV. As we do not know exactly the value of the Coulomb repulsion on the Te site, we estimated the enhancement for U_p in the range from 2 eV to 8 eV, which seem plausible values.

Our results in Fig. S17 show that an enhancement of the superexchange interaction and hence the Curie temperature of more than threefold can be expected. We now use our measured values of the charge-transfer gap from Fig. 1(d) in the main text to estimate the enhancement factor for the superexchange interaction as a function of pressure. Our results for the enhancement factor in Fig. S18 show a strong pressure dependence. While the end point of this curve at high pressures fits the experimentally confirmed enhancement of the Curie temperature by a factor of roughly three in the same pressure range quite well, it is not yet clear whether the pressure dependence for the Curie temperature is reproduced well.

To verify the pressure dependence we use the previously calculated enhancement factors (at $U_p = 7$ eV) as a function of pressure and multiply them by a base Curie temperature of 55 K. Subsequently, we plot these values together with the experimental values and the double-exchange model. The results are shown in Fig. S19.

Although the superexchange (SE) model delivers the correct order of magnitude for the Curie temperature at high pressures, several aspects speak against explaining the increased T_{C} in terms of superexchange: (i) the quantitative fit of the experimental data is way worse than for the DE model, (ii) the SE model should describe T_{C} across the insulator-to-metal transition, but especially the region close to the transition is where deviations are largest; (iii) the model is based on a single exchange path, while the known magnetic Hamiltonian for $CrGeTe_3$ also contains long-range couplings [6]. All of these points call the validity of the simple superexchange model into question.

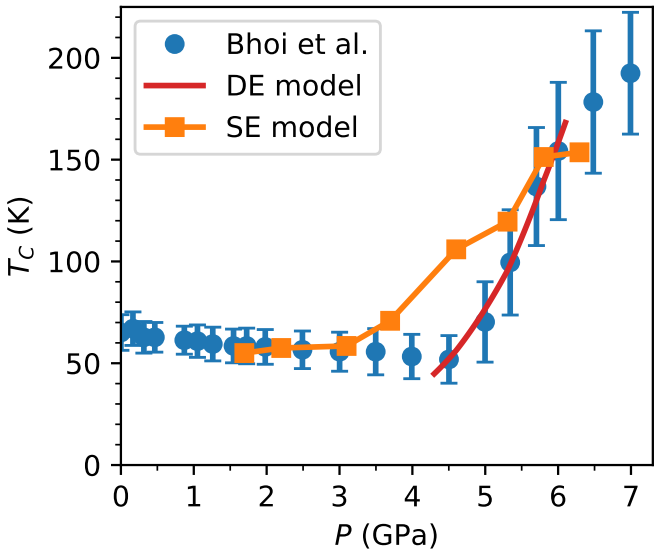

FIG. S19. Experimental Curie temperature as a function of pressure from Ref. [2] along with theoretical estimates from the (linear in ω_{p}^2) double-exchange (DE) model and the suggested superexchange (SE) model at $U_p = 7$ eV, which depends on the inverse of the optical gap.

While the superexchange model cannot be discarded completely due to its roughly correct enhancement factor for T_{C}, we believe in conclusion that the double-exchange model currently delivers the best explanation of the enhanced Curie temperature in metallic $CrGeTe_3$ under pressure.

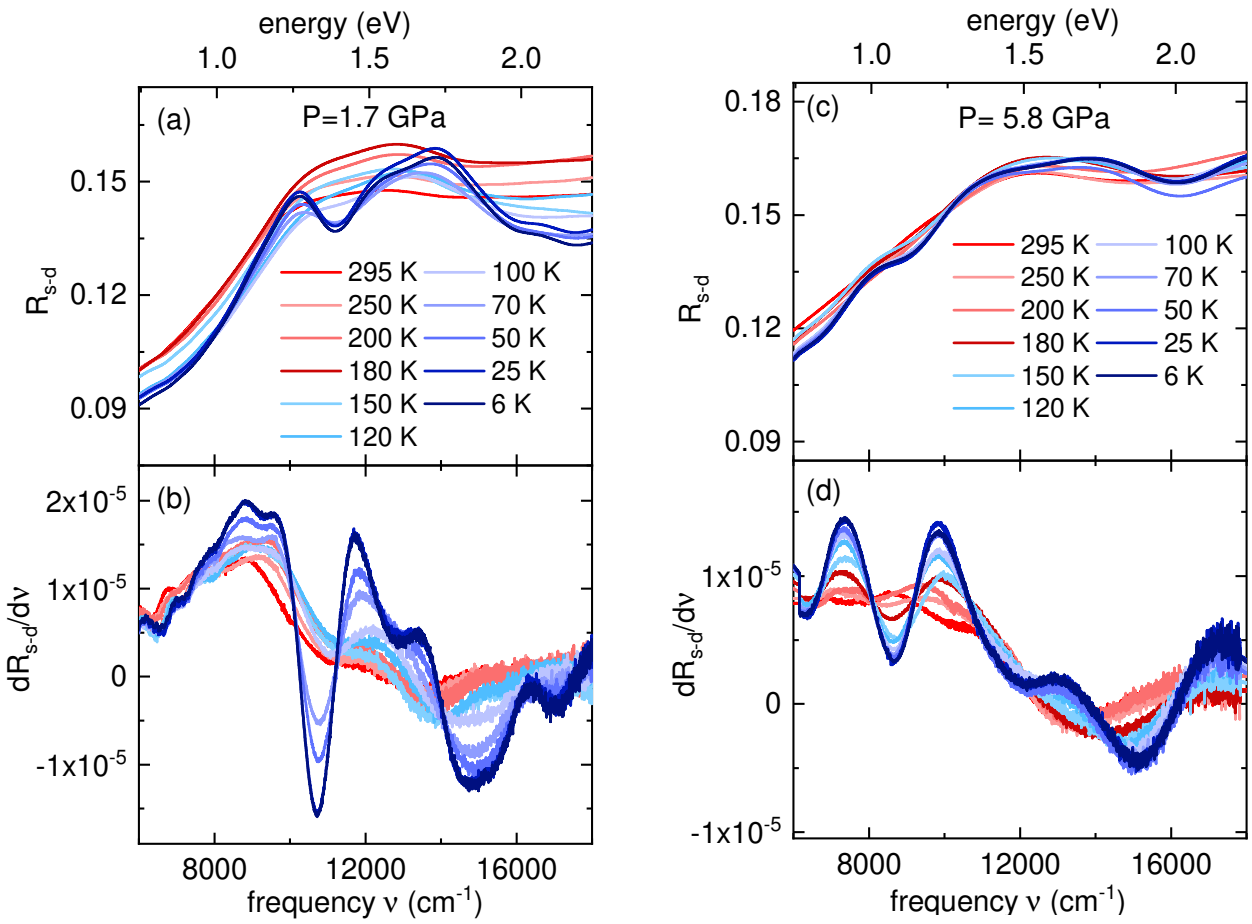

FIG. S20. High-energy reflectivity spectrum R_{s-d} of $CrGeTe_3$ at 1.7 GPa (a) and at 5.8 GPa (c) together with the corresponding first derivative $dR_{s-d}/d\nu$ at 1.7 GPa (b) and at 5.8 GPa (d).

VIII. EXPERIMENTAL ESTIMATE OF MASS ENHANCEMENT

We can furthermore trace the strength of electronic correlations based on the experimental optical conductivity spectrum. The extraction of the electronic correlation strength from optical conductivity spectra is an established procedure applied to various quantum materials [46–48]. The optical conductivity spectrum of $CrGeTe_3$ in the high-pressure (either paramagnetic or ferromagnetic) metallic phase contains an MIR absorption band, which, according to our theoretical calculations, is attributed to electronic correlation effects. The spectral weights of the MIR band and the Drude term can serve as a measure for the electronic correlation strength, as explained below. This gives us the unique possiblity to trace the correlation strength as a function of pressure in a 2D vdW material.

The Drude spectral weight ω_p^2 serves as an estimate of the optical kinetic energy K_{opt} of the quasiparticles, and its reduction as compared to its value K_{band} obtained from non-interacting band theory calculations is a measure of the electronic correlation strength [46–48]. The ratio K_{opt}/K_{band} can be estimated from the experimental plasma frequency ω_p of the Drude term and the oscillator strength Ω_{MIR} of the MIR band according to [47]

$$\text{ratio}_{corr} = \frac{K_{opt}}{K_{band}} \approx \frac{\omega_p^2}{\omega_p^2 + \Omega_{MIR}^2} \quad . \tag{10}$$

The value of ratio_{corr} ranges between 0 (Mott insulator) and 1 (uncorrelated metal). It corresponds to the quasiparticle weight calculated in Section IV.

In case of $CrGeTe_3$, the so-obtained value of ratio_{corr} as a function of pressure at 25 K is shown in Fig. 1(d) in the main text. At P_c, ratio_{corr} rises sharply and saturates at the value 0.7 above 4.6 GPa Accordingly, $CrGeTe_3$ in its metallic phase is moderately correlated, similar to the square-net nodal-line semimetal ZrSiSe and slightly less correlated than the ferromagnetic kagome metal $Co_3Sn_2S_2$ [46]. In comparison, for strongly correlated metals such as cuprates and the vanadium oxide V_2O_3 a value $\text{ratio}_{corr} \sim 0.2$ would be expected [48] (see also Table S1 for a comparison with other vdW materials).

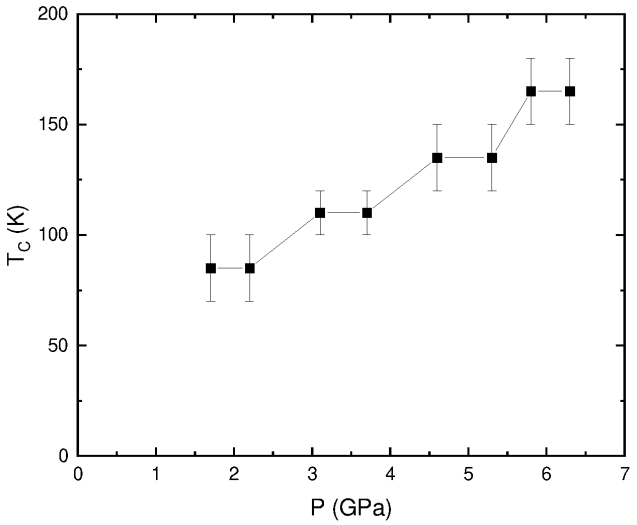

FIG. S21. Ferromagnetic ordering temperature T_C of $CrGeTe_3$ as a function of pressure as obtained from the optical data.

IX. ESTIMATE OF THE CURIE TEMPERATURE FROM OPTICAL DATA

When entering the ferromagnetic state during cooling, significant changes occur in the high-energy reflectivity spectrum R_{s-d}, as illustrated in Figs. S20(a) and (c) for P=1.7 GPa and P=5.8 GPa, respectively. These temperature-induced changes appear even more clearly in the first derivative of the reflectivity with respect to frequency $dR_{s-d}/d\nu$ [see Figs. S20(b) and (d)]. For example, at 1.7 GPa a clear dip feature develops in $dR_{s-d}/d\nu$ at ∼10800 cm^{-1} between 100 and 70 K [Fig. S20(b)]. Accordingly, magnetic order sets in below 100 K, and we can estimate the Curie temperature T_C=85 K ± 15 K at 1.7 GPa. Applying this criterion to all measured pressures, we obtained the pressure dependence of the magnetic ordering temperature T_C as depicted in Fig. S21.

X. DECOMPOSITIONS OF THE σ_1 SPECTRA AS A FUNCTION OF PRESSURE AND TEMPERATURE

The decompositions of the σ_1 spectra as a function of pressure and temperature are shown in Figs. S22, S23, S24, and S25.

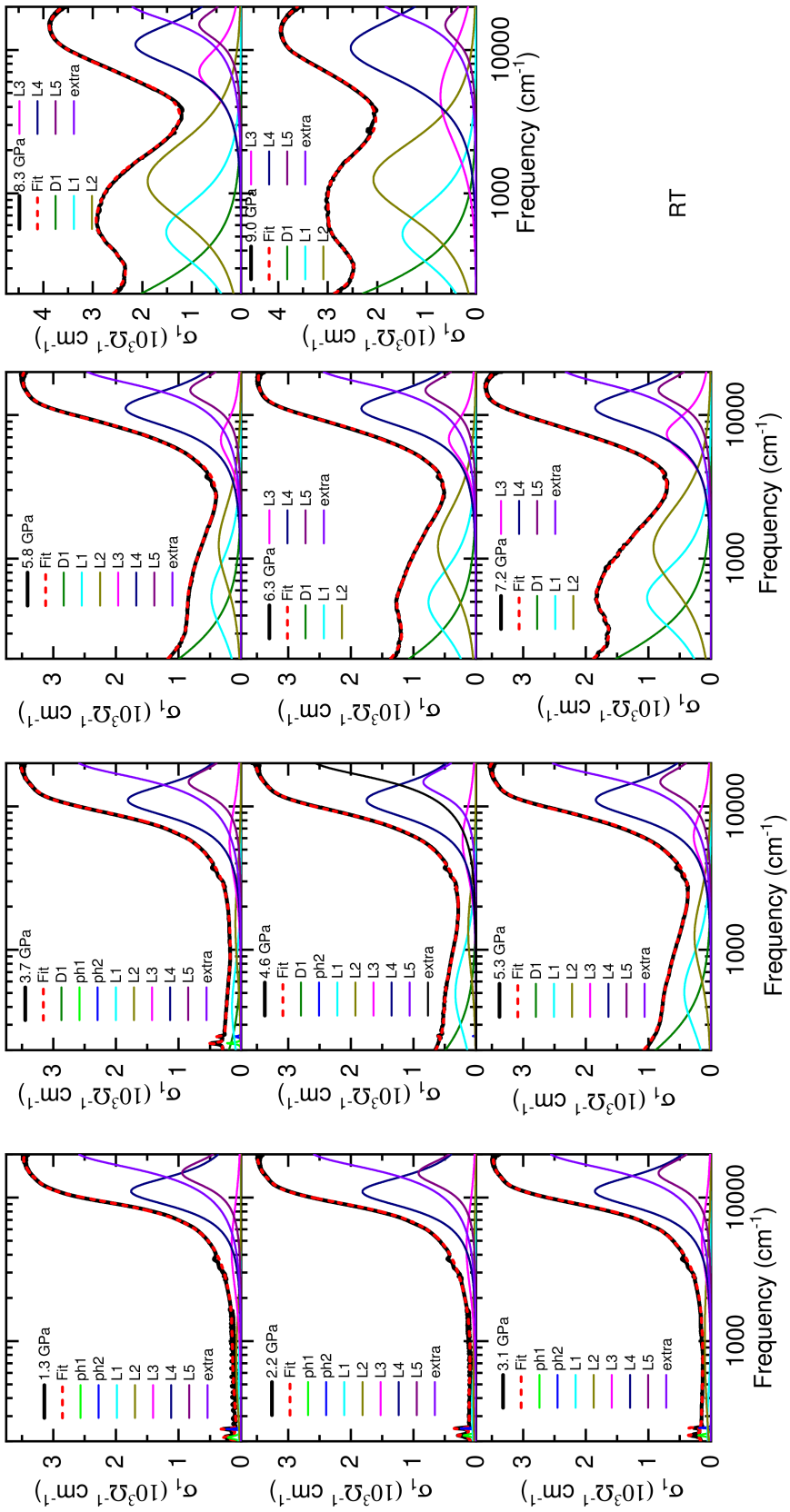

FIG. S22. Decompositions of the σ_1 spectra as a function of pressure at room temperature.

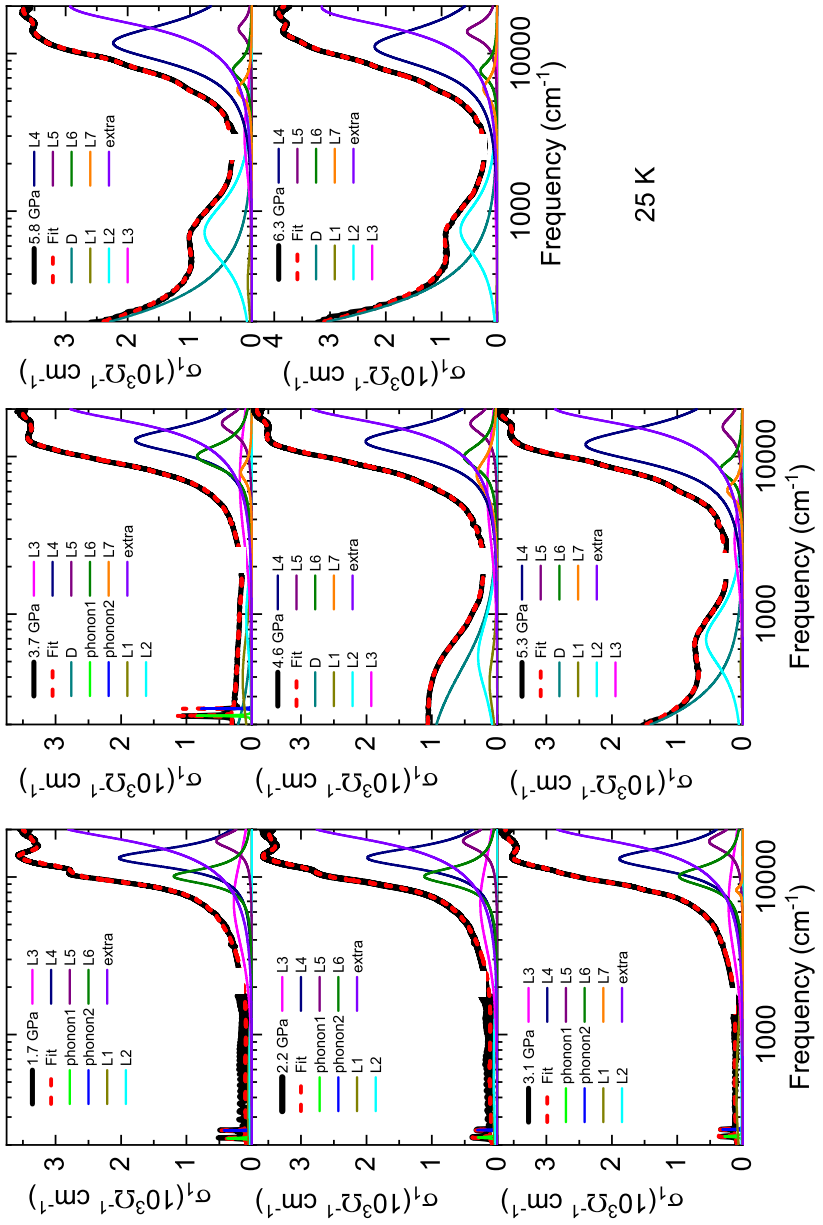

FIG. S23. Decompositions of the σ_1 spectra as a function of pressure at 25 K.

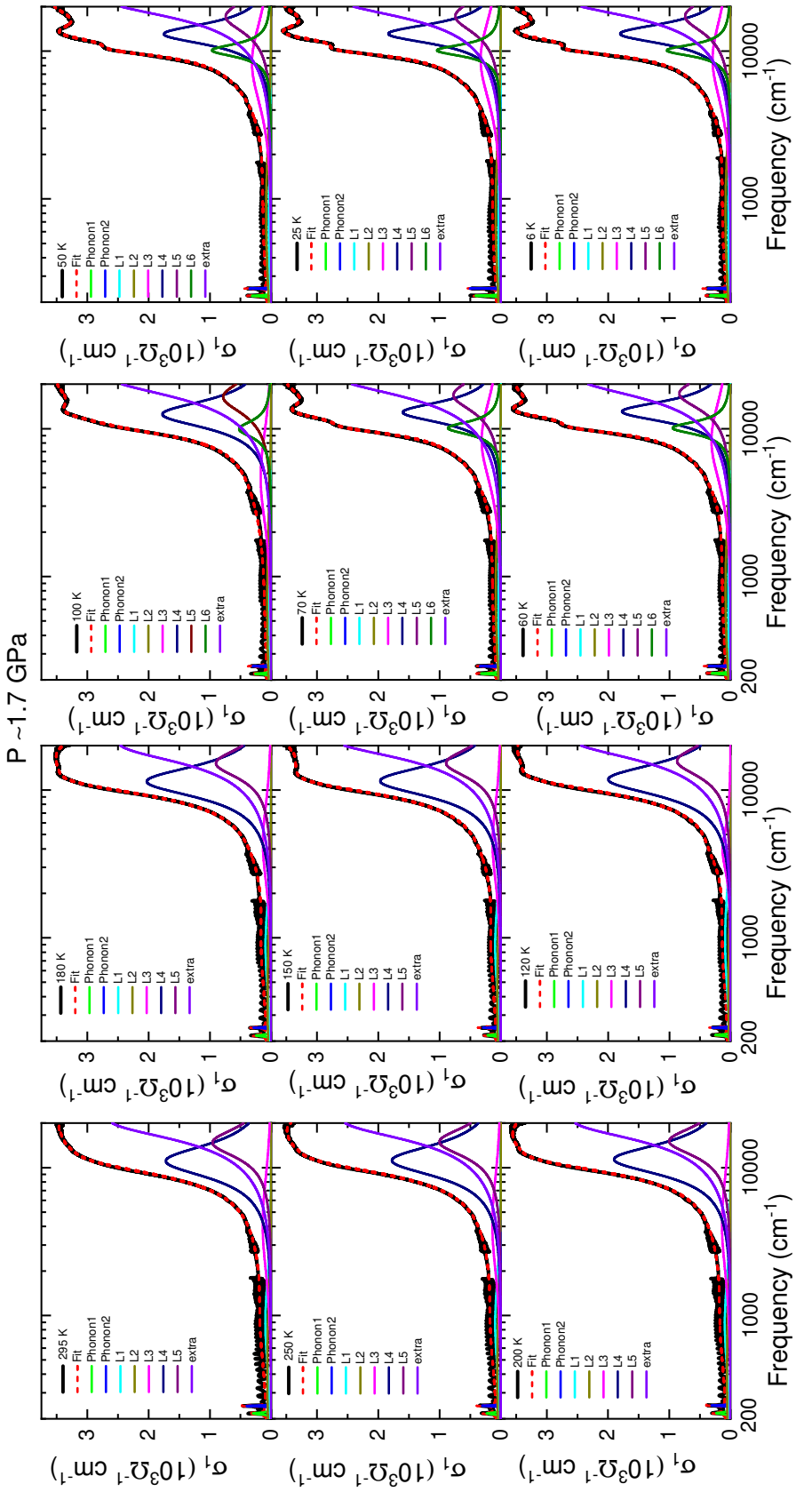

FIG. S24. Decompositions of the σ_1 spectra as a function of temperature at ~1.7 GPa.

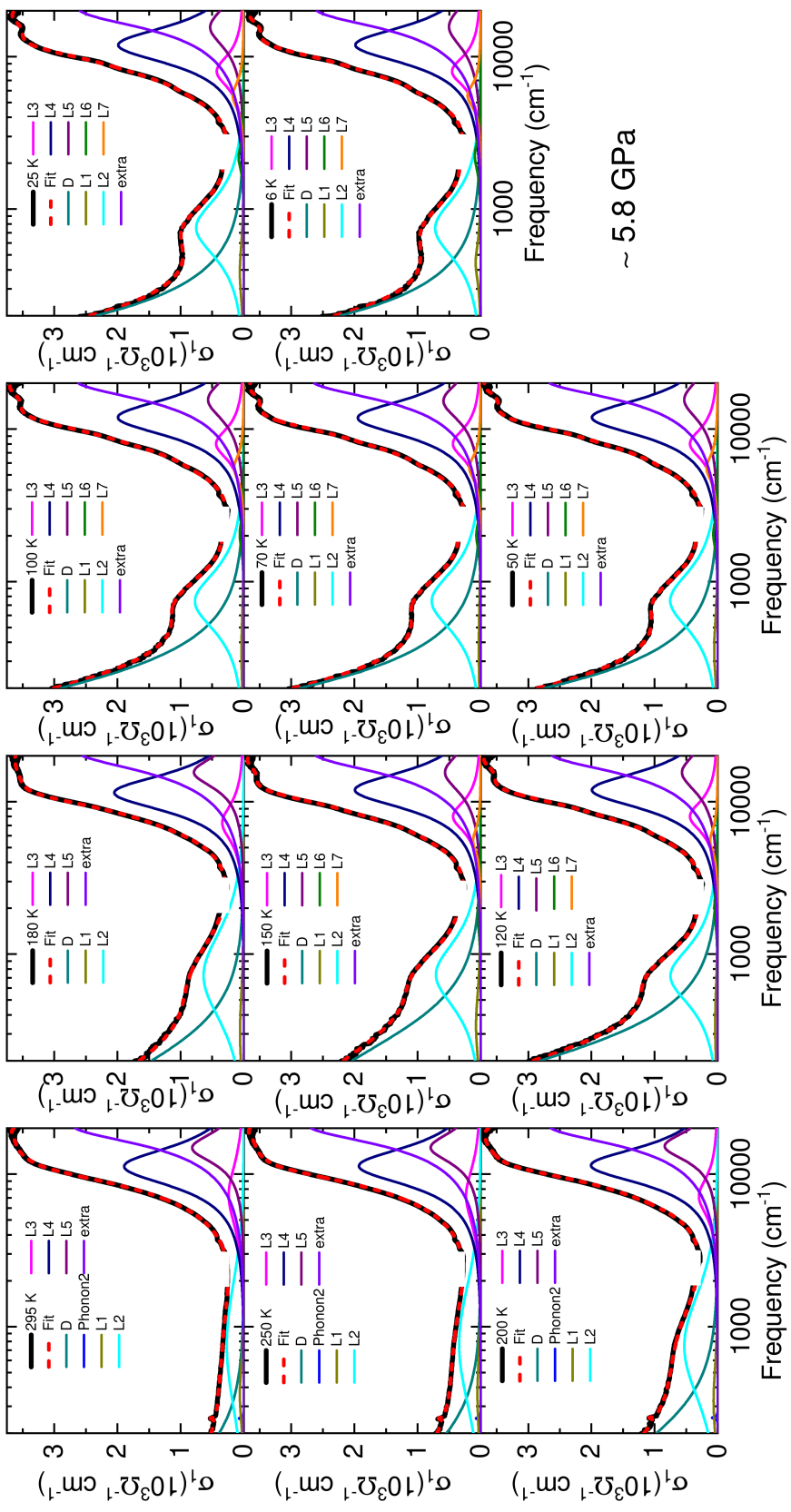

FIG. S25. Decompositions of the σ_1 spectra as a function of temperature at ~5.8 GPa.

[1] H. Ji, R. A. Stokes, L. D. Alegria, E. C. Blomberg, M. A. Tanatar, A. Reijnders, L. M. Schoop, T. Liang, R. Prozorov, K. S. Burch, N. P. Ong, J. R. Petta, and R. J. Cava, A ferromagnetic insulating substrate for the epitaxial growth of topological insulators, J. Appl. Phys. **114**, 114907 (2013).

[2] D. Bhoi, J. Gouchi, N. Hiraoka, Y. Zhang, N. Ogita, T. Hasegawa, K. Kitagawa, H. Takagi, K. H. Kim, and Y. Uwatoko, Nearly room-temperature ferromagnetism in a pressure-induced correlated metallic state of the van der Waals insulator $CrGeTe_3$, Phys. Rev. Lett. **127**, 217203 (2021).

[3] V. Carteaux, D. Brunet, G. Ouvrard, and G. Andre, Crystallographic, magnetic and electronic structures of a new layered ferromagnetic compound $Cr_2Ge_2Te_6$, J. Phys.: Condens. Matter **7**, 69 (1995).

[4] M. D. Watson, I. Marković, F. Mazzola, A. Rajan, E. A. Morales, D. M. Burn, T. Hesjedal, G. van der Laan, S. Mukherjee, T. K. Kim, C. Bigi, I. Vobornik, M. Ciomaga Hatnean, G. Balakrishnan, and P. D. C. King, Direct observation of the energy gain underpinning ferromagnetic superexchange in the electronic structure of $CrGeTe_3$, Phys. Rev. B **101**, 205125 (2020).

[5] J. Zhang, X. Cai, W. Xia, A. Liang, J. Huang, C. Wang, L. Yang, H. Yuan, Y. Chen, S. Zhang, Y. Guo, Z. Liu, and G. Li, Unveiling electronic correlation and the ferromagnetic superexchange mechanism in the van der Waals crystal $CrSiTe_3$, Phys. Rev. Lett. **123**, 047203 (2019).

[6] H.-X. Xu, M. Shimizu, D. Guterding, J. Otsuki, and H. O. Jeschke, Pressure evolution of electronic structure and magnetism in the layered van der Waals ferromagnet $CrGeTe_3$, Phys. Rev. B **108**, 125142 (2023).

[7] H. K. Mao, J. Xu, and P. M. Bell, Calibration of the ruby pressure gauge to 800 kbar under quasi-hydrostatic conditions, J. Geophys. Res. **91**, 4673 (1986).

[8] K. Syassen, Ruby under pressure, High Pressure Res. **28**, 75 (2008).

[9] M. I. Eremets and Y. A. Timofeev, Miniature diamond anvil cell: Incorporating a new design for anvil alignment, Rev. Sci. Instrum. **63**, 3123 (1992).

[10] J. Ebad-Allah, M. Krottenmüller, J. Hu, Y. L. Zhu, Z. Q. Mao, and C. A. Kuntscher, Infrared spectroscopy study of the nodal-line semimetal candidate ZrSiTe under pressure: Hints for pressure-induced phase transitions, Phys. Rev. B **99**, 245133 (2019).

[11] J. Ebad-Allah, S. Rojewski, M. Vöst, G. Eickerling, W. Scherer, E. Uykur, R. Sankar, L. Varrassi, C. Franchini, K.-H. Ahn, J. Kuneš, and C. A. Kuntscher, Pressure-induced excitations in the out-of-plane optical response of the nodal-line semimetal ZrSiS, Phys. Rev. Lett **127**, 076402 (2021).

[12] J. Ebad-Allah, S. Rojewski, Y. L. Zhu, Z. Q. Mao, and C. A. Kuntscher, In-plane and out-of-plane optical response of the nodal-line semimetals ZrGeS and ZrGeSe, Phys. Rev. B **106**, 075143 (2022).

[13] D. B. Tanner, Use of x-ray scattering functions in Kramers-Kronig analysis of reflectance, Phys. Rev. B **91**, 035123 (2015).

[14] Y. Lu, H. Kono, T. Larkin, A. Rost, T. Takayama, A. V. Boris, B. Keimer, and H. Takagi, Zero-gap semiconductor to excitonic insulator transition in Ta_2NiSe_5, Nature Commun. **8**, 14408 (2017).

[15] E. Uykur, R. Sankar, D. Schmitz, and C. A. Kuntscher, Optical spectroscopy study on pressure-induced phase transitions in the three-dimensional Dirac semimetal Cd_3As_2, Phys. Rev. B **97**, 195134 (2018).

[16] R. Yang, M. Corasaniti, L. Wu, Q. Du, Y. Zhu, C. Petrovic, and L. Degiorgi, Ingredients for enhanced thermoelectric power at cryotemperatures in the correlated semiconductor CoSbS revealed by its optical response, Phys. Rev. B **103**, L161111 (2021).

[17] M. Köpf, S. H. Lee, Z. Q. Mao, and C. A. Kuntscher, Optical study of the charge dynamics evolution in the topological insulators $MnBi_2Te_4$ and $Mn(Bi_{0.74}Sb_{0.26})_2Te_4$ under high pressure, Phys. Rev. B **109**, 245124 (2024).

[18] K. Koepernik and H. Eschrig, Full-potential nonorthogonal local-orbital minimum-basis band-structure scheme, Phys. Rev. B **59**, 1743 (1999).

[19] J. P. Perdew, K. Burke, and M. Ernzerhof, Generalized gradient approximation made simple, Phys. Rev. Lett. **77**, 3865 (1996).

[20] Z. Yu, W. Xia, K. Xu, M. Xu, H. Wang, X. Wang, N. Yu, Z. Zou, J. Zhao, L. Wang, X. Miao, and Y. Guo, Pressure-induced structural phase transition and a special amorphization phase of two-dimensional ferromagnetic semiconductor $Cr_2Ge_2Te_6$, J. Phys. Chem. C **123**, 13885 (2019).

[21] Y. Fang, S. Wu, Z.-Z. Zhu, and G.-Y. Guo, Large magneto-optical effects and magnetic anisotropy energy in two-dimensional $Cr_2Ge_2Te_6$, Phys. Rev. B **98**, 125416 (2018).

[22] H. Shinaoka, J. Otsuki, M. Kawamura, N. Takemori, and K. Yoshimi, DCore: Integrated DMFT software for correlated electrons, SciPost Phys. **10**, 117 (2021).

[23] H. Eschrig and K. Koepernik, Tight-binding models for the iron-based superconductors, Phys. Rev. B **80**, 104503 (2009).

[24] P. Werner, A. Comanac, L. de' Medici, M. Troyer, and A. J. Millis, Continuous-time solver for quantum impurity models, Phys. Rev. Lett. **97**, 076405 (2006).

[25] E. Gull, A. J. Millis, A. I. Lichtenstein, A. N. Rubtsov, M. Troyer, and P. Werner, Continuous-time Monte Carlo methods for quantum impurity models, Rev. Mod. Phys. **83**, 349 (2011).

[26] J. Otsuki, K. Yoshimi, H. Shinaoka, and H. O. Jeschke, Multipolar ordering from dynamical mean field theory with application to CeB_6, Phys. Rev. B **110**, 035104 (2024).

[27] M. Aichhorn, L. Pourovskii, P. Seth, V. Vildosola, M. Zingl, O. E. Peil, X. Deng, J. Mravlje, G. J. Kraberger, C. Martins, M. Ferrero, and O. Parcollet, TRIQS/DFTTools: A TRIQS application for ab initio calculations of correlated materials, Comput. Phys. Commun. **204**, 200 (2016).

[28] `https://github.com/j-otsuki/cthyb`.

[29] H. Kajueter, G. Kotliar, and G. Moeller, Doped Mott insulator: Results from mean-field theory, Phys. Rev. B **53**, 16214 (1996).

[30] O. Parcollet and A. Georges, Non-Fermi-liquid regime of a doped Mott insulator, Phys. Rev. B **59**, 5341 (1999).

[31] B. Kyung, S. S. Kancharla, D. Sénéchal, A.-M. S. Tremblay, M. Civelli, and G. Kotliar, Pseudogap induced by

short-range spin correlations in a doped Mott insulator, Phys. Rev. B **73**, 165114 (2006).
[32] D. E. Logan and M. R. Galpin, Mott insulators and the doping-induced Mott transition within DMFT: exact results for the one-band Hubbard model, J. Phys. Condens. Matter **28**, 025601 (2015).
[33] A. A. Katanin, A. P. Kampf, and V. Y. Irkhin, Anomalous self-energy and Fermi surface quasisplitting in the vicinity of a ferromagnetic instability, Phys. Rev. B **71**, 085105 (2005).
[34] H. J. Vidberg and J. W. Serene, Solving the Eliashberg equations by means of N-point Padé approximants, J. Low Temp. Phys. **29**, 179 (1977).
[35] J. Otsuki, M. Ohzeki, H. Shinaoka, and K. Yoshimi, Sparse modeling in quantum many-body problems, J. Phys. Soc. Jpn. **89**, 012001 (2020).
[36] T. J. Kim, S. Ryee, M. J. Han, and S. Choi, Dynamical mean-field study of vanadium diselenide monolayer ferromagnetism, 2D Mater. **7**, 035023 (2020).
[37] H. Fujiwara, K. Terashima, J. Otsuki, N. Takemori, H. O. Jeschke, T. Wakita, Y. Yano, W. Hosoda, N. Kataoka, A. Teruya, M. Kakihana, M. Hedo, T. Nakama, Y. Ōnuki, K. Yaji, A. Harasawa, K. Kuroda, S. Shin, K. Horiba, H. Kumigashira, Y. Muraoka, and T. Yokoya, Anomalously large spin-dependent electron correlation in the nearly half-metallic ferromagnet CoS_2, Phys. Rev. B **106**, 085114 (2022).
[38] B. G. Jang, G. Han, I. Park, D. Kim, Y. Y. Koh, Y. Kim, W. Kyung, H.-D. Kim, C.-M. Cheng, K.-D. Tsuei, K. D. Lee, N. Hur, J. H. Shim, C. Kim, and G. Kotliar, Direct observation of kink evolution due to Hund's coupling on approach to metal-insulator transition in $NiS_{2-x}Se_x$, Nat. Commun. **12**, 1208 (2021).
[39] Y. Wang, C.-J. Kang, H. Miao, and G. Kotliar, Hund's metal physics: From $SrNiO_2$ to $LaNiO_2$, Phys. Rev. B **102**, 161118 (2020).
[40] I. Leonov, S. L. Skornyakov, and S. Y. Savrasov, Lifshitz transition and frustration of magnetic moments in infinite-layer $NdNiO_2$ upon hole doping, Phys. Rev. B **101**, 241108 (2020).
[41] C.-J. Kang, J. Hong, and J. Kim, Dynamical mean-field theory study of a ferromagnetic CrI_3 monolayer, J. Korean Phys. Soc. **80**, 1071 (2022).
[42] L.-F. Arsenault, P. Sémon, and A.-M. S. Tremblay, Benchmark of a modified iterated perturbation theory approach on the fcc lattice at strong coupling, Phys. Rev. B **86**, 085133 (2012).
[43] C.-J. Kang and G. Kotliar, Optical properties of the infinite-layer $La_{1-x}Sr_xNiO_2$ and hidden Hund's physics, Phys. Rev. Lett. **126**, 127401 (2021).
[44] V. M. Pereira, J. M. B. Lopes dos Santos, E. V. Castro, and A. H. Castro-Neto, Double exchange model for magnetic hexaborides, Phys. Rev. Lett. **93**, 147202 (2004).
[45] P. W. Anderson and H. Hasegawa, Considerations on double exchange, Phys. Rev. **100**, 675 (1955).
[46] Y. Shao, A. N. Rudenko, J. Hu, Z. Sun, Y. Zhu, S. Moon, A. J. Millis, S. Yuan, A. I. Lichtenstein, D. Smirnov, Z. Q. Mao, M. I. Katsnelson, and D. N. Basov, Electronic correlations in nodal-line semimetals, Nat. Phys. **16**, 636 (2020).
[47] L. Degiorgi, Electronic correlations in iron-pnictide superconductors and beyond: lessons leaned from optics, New J. Phys. **13**, 023011 (2011).
[48] M. M. Qazilbash, J. J. Hamlin, R. E. Baumbach, L. Zhang, D. J. Singh, M. B. Maple, and D. N. Basov, Electronic correlations in the iron pnictides, Nat. Phys. **5**, 647 (2009).